Inorganic Chemistry Communications 174 (2025) 113919

Contents lists available at ScienceDirect

Inorganic Chemistry Communications

journal homepage: www.elsevier.com/locate/inoche

Research Article

New Insights into the application of Copper-Based polymer composites as Catalysts: An Indepth experimental and computational study

Nazli Turkten [a], Yunus Karatas [a,*], Yelda Yalcin Gurkan [b]

[a] Department of Chemistry, Faculty of Arts and Sciences, Kirsehir Ahi Evran University, Kirsehir 40100 Türkiye
[b] Department of Chemistry, Faculty of Arts and Sciences, Tekirdag Namik Kemal University, Tekirdag 59030 Türkiye

ARTICLE INFO

Keywords:
Conceptual Density Functional Theory
PANI-CuO composites
Photocatalysis
Reactive Orange 122
Recyclability tests

ABSTRACT

A series of polyaniline-copper oxide (PANI-CuO) composites were synthesized using *in-situ* chemical oxidation polymerization (PCI) and mechano-chemical preparation (PCS) methods. The influence of the synthesis methods on the morphological, structural, surface, thermal, and optical properties of the composites was systematically investigated. Characterization techniques including Fourier transformer infrared (FTIR), Raman spectroscopy, X-ray diffraction (XRD), scanning electron microscopy (SEM), thermal gravimetric (TG), and differential thermal analysis (DTA), and photoluminescence (PL) were employed to confirm the formation of the composites and analyze their structural features. The morphology of the PANI-CuO composites was found to be dependent on the PANI/CuO ratio and the synthesis method. XRD revealed the semi-crystalline nature of PANI and the monoclinic structure of CuO. Photocatalytic performance was evaluated by the degradation of anionic Reactive Orange-122 (RO-122) dye with the PCS-81 composite achieving 91 % degradation of RO-122 in 120 min. Recyclability tests demonstrated high stability of the composites, suggesting their potential as efficient photocatalysts for dye removal from aqueous solutions. FTIR, Raman, and SEM analyses were used to monitor morphological and structural changes during RO-122 photodegradation. Conceptual Density Functional Theory (CDFT) calculations were also performed to identify reactive sites for hydroxyl radical attack, and reactivity descriptors were calculated using the DFT/B3LYP/6-31G(d) method. A photocatalytic degradation mechanism for RO-122 was proposed by integrating computational and experimental data.

1. Introduction

Nowadays, controlling water pollution associated with the rigorous growth of industrialization containing synthetic dyes has become a top priority [1]. Among synthetic dyes, reactive dyes are particularly utilized in the textile industry, predominantly dyeing cotton and cellulosic fibers and fabrics containing small amounts of silk and wool fibers [2,3]. RO-122 is an example of an anionic reactive dye presenting a complex chemical structure with an azo group linked to naphthalene rings. Researchers have reported limited experimental data on the removal of RO-122 dye, including adsorption [4,5], biodegradation [6], biosorption [7,8], Fenton [9], ozonation [10], photocatalysis [11–18]. For environmental remediation and to prevent undesirable detrimental consequences associated with humans and aquatic life, adequate treatment of dye-containing wastewater from industries before discharge is essential [2,19].

Conventional techniques and combinations of biological, physical, and chemical processes have exhibited several limitations leading to high operational costs and insufficient degradation of highly structured dye molecules [2]. Among the water treatment technologies, heterogeneous photocatalysis in the realm of photochemistry is based on unique chemical transformations that generate highly oxidizing species. In addition, this environmentally promising and enhanced oxidizing phenomenon is used for treating effluents of recalcitrant compounds under moderate conditions and offers no secondary pollution [20,21].

Up to date, TiO_2, ZnO, and graphene-based photocatalysts have received considerable interest in designing new catalytic materials [22–27]. Fatima et al. prepared TiO_2-based nanostructured materials using surfactants such as tannic acid, decyltrimethylammonium bromide, and tetraoctylphosphonium bromide [22]. In another study, a novel ZnO/reduced graphene oxide-based photocatalyst was prepared and the catalytic activity was tested on the degradation of rose bengal dye [25]. Ghumro et al. prepared carbon-doped titania nanostructures via a facile hydrothermal route using carbon sources, i.e., carbon sheets,

* Corresponding author.
E-mail address: ykaratas@ahievran.edu.tr (Y. Karatas).

https://doi.org/10.1016/j.inoche.2025.113919
Received 30 November 2024; Received in revised form 25 December 2024; Accepted 5 January 2025
Available online 17 January 2025

acetylene black, graphene oxide, and reduced graphene oxide [24].

Recently, transition metal oxides-based benchmark photocatalysts have been considered for removing dyes from water [28]. CuO is a p-type semiconductor that comprises such benefits as low cost, non-toxic, a narrow band gap (1.7 eV), and efficient electron transfer [29,30]. However, the major drawback suppressing the photocatalytic efficiency of CuO is associated with the possibility of fast recombination of photogenerated electron-hole charge carriers [31]. Hence, up to now, the design of polymer-based CuO materials has attracted attention as novel surface-engineered photocatalysts [32–35]. Among polymer network materials, conjugated polymers (CPs) with coupling semiconductors are a better choice since an extended π-conjugated system efficiently suppresses electron-hole recombination, thereby providing a synergic effect to enhance photocatalytic activity [36].

CPs used in photocatalysis today are mainly PANI, polypyrrole, and polythiophene composites, which have attracted attention as novel surface-engineered photocatalysts [37–41]. PANI is a relatively inexpensive p-type material compared to other CPs, featuring ease of synthesis and containing repeated benzenoid and quinoid units. The outstanding environmentally stable polymer with π-bonds on its backbone contains nitrogen atoms in amine and imine functional groups that can enable the effective adsorption of pollutants in water treatment. The main strategy of constructing PANI-based composites with semiconductors is often used to improve the photogenerated electron/hole separation and enhance photocatalytic activity [42–45]. Among inorganic oxides, TiO_2 and ZnO are extensively prepared semiconductors combined with PANI for photocatalytic degradation [39]. Notably, the application of *in-situ* oxidative polymerization and hybridization methods, in the synthesis of PANI-TiO_2 and PANI-ZnO, as polymer-modified photocatalysts have been investigated in our previous studies [46–48]. In addition, although PANI-TiO_2 and PANI-ZnO composites have been widely investigated, there are only a few reports on the photocatalytic performance of PANI-CuO composites [42].

So far, not many studies on doped-PANI-CuO composites and other material-based PANI-CuO composites used for photocatalytic degradation of dyes and organic pollutants have been reported [49–53]. Nekooie and co-workers prepared a CuO-TiO_2-PANI nanocomposite to degrade the toxic pesticide chlorpyrifos in water [51]. Rathore et al. used chitosan-PANI-CuO nanocomposite as a photocatalyst to remove methyl orange and almost all of the dye was degraded [52]. In another photocatalytic study, the degradation of congo red in the presence of chitosan/hydroxyethyl cellulose gel immobilized PANI-CuO-ZnO hybrid nanocomposite was investigated [53].

The common technique used for the fabrication of PANI-CuO composites is *in-situ* chemical oxidative polymerization, which mostly involves oxidative polymerization of aniline monomer with ammonium persulphate (APS) as the initiator. In this method, HCl [54–58] was preferentially used as a dopant/acid medium to prepare PANI-CuO composites in an aqueous solution; also oxalic acid [59], H_2SO_4 [60], citric acid [61,62], and acetic acid [63], were used alternatively. Recently, a mechanochemical method has been preferred over existing techniques for preparing PANI-CuO composites because of its simplicity and low energy consumption. This effective method comprises mechanical mixing of PANI and CuO separately in water. [64–66].

Although most studies on photocatalysis are based on the assessment of the photocatalytic efficiency of organic pollutants, only a few reports have examined the plausible photocatalytic degradation mechanism of dyes and antibiotics using combined computational and experimental chemistry [67,68]. Gurkan et al. proposed a possible photocatalytic degradation mechanism of cefazolin by applying quantum mechanical calculations within the framework of Conceptual Density Functional Theory (CDFT) [67]. Furthermore, the predicted mechanism of cefazolin was confirmed by the experimental results reported in the literature. In another CDFT study, comprehensive data about the reactivity sites of an azo dye were predicted using the Fukui function for radical attacks. The photocatalytic degradation mechanism of Reactive Red 195 was determined by experimental FTIR and GC–MS analysis with the use of Density Functional Theory (DFT) [68].

In this paper, a series of PANI-CuO composites with three different PANI amounts were comparatively prepared by *in-situ* polymerization and mechanical methods. The known fact that copper oxide dissolves in acidic media has been overlooked in some studies in the community. This fact was examined systematically and comparatively in one of the two different composite preparation methods used here. In parallel, a comprehensive study was carried out on the differences of PANI-CuO composites with various characterization techniques. The morphological, structural, optical, and thermal properties of the composites obtained by the two methods have been identified using SEM, XRD, FTIR, Raman spectroscopy, and TG/DTA techniques. To the best of our knowledge, systematic preparation and characterization of PANI-CuO composites via two routes have not been reported at present. Finally, the photocatalytic degradation of RO-122 in the presence of PANI-CuO composites was also performed experimentally to compare with the computational results. In the computational part, the photocatalytic degradation mechanism of RO-122 was proposed and discussed for the first time using Fukui functions. All theoretical calculations were performed by utilizing DFT/B3LYP/6-31G(d) method. As distinct from the photocatalytic studies of polymeric composites in literature, this study offered combined experimental and computational data to fill this knowledge gap.

2. Methodology

2.1. Materials

Copper(II) oxide (CuO, ACS, Thermo Scientific), aniline (ANI, $C_6H_5NH_2$, for analysis), ammonium persulfate (APS, $(NH_4)_2S_2O_8$, ACS reagent, ≥98.0 %, Merck), and hydrochloric acid (HCl, ACS reagent, 37 %, Merck) were used without further purification. Reactive Orange 122 (RO-122, $C_{31}H_{20}ClN_7Na_4O_{16}S_5$) dye was used as a model pollutant. All aqueous solutions were prepared with deionized water (conductivity < 1 μS/cm at 25 °C).

2.2. Preparation of PANI and PANI-CuO composites

Polyaniline emeraldine salt was synthesized by *in-situ* chemical oxidation polymerization method and referred to simply as PANI. PANI-CuO composites were prepared via the mechano-chemical preparation method labeled as PCS composites and *in-situ* chemical oxidation polymerization method labeled as PCI composites.

2.2.1. Preparation of PANI

PANI was synthesized by *in-situ* chemical oxidation polymerization method as reported in our previous study [47]. Briefly, 2.33 g (25 mmol) of ANI monomer was added slowly into 80 mL HCl (1 M) solution in an ice bath under magnetic stirring. After that, 5.71 g (25 mmol) APS in 80 mL HCl (1 M) solution was added dropwise (approximately one drop/second) into the above monomer mixture under stirring and then kept in a stirring condition for 24 h at room temperature. The resulting dark green composite was filtered and thoroughly washed with distilled water and ethanol to remove unreacted monomers or oligomers. The final product was dried in an air oven at 80 °C for 24 h.

2.2.2. Mechano-Chemical preparation method

PANI-CuO composites were synthesized by the mechano-chemical preparation method proposed by Maruthi and colleagues [65]. CuO and synthesized PANI (as described above) were added to 50 mL of distilled water and stirred well for 24 h. In the next step, the mixture was filtered, and the resulting product was subsequently washed with distilled water. The PCS composites obtained were dried in an air oven at 80 °C for 24 h. The mole ratios of PANI/CuO were 1:8, 1:1, and 8:1 and these PCS composites were named PCS-18, PCS-11, and PCS-81,

respectively.

2.2.3. In-situ chemical oxidation polymerization method

PANI-CuO composites were synthesized by *in-situ* chemical oxidation polymerization method with a minor modification and referred to as PCI composites [47]. PCI composites were prepared at the initial ANI/CuO mole ratios of 1:8, 1:1, and 8:1 and these composites were labeled as PCI-18, PCI-11, and PCI-81, respectively. The initial mole ratio of ANI/APS was 1:1 in all composites and the representative synthesis of PCI-11 was given as follows: At first, 5.71 g (25 mmol) of APS was dissolved in 80 mL of 1 M HCl solution and placed in a dropping funnel (Solution A). Solution B was obtained by adding 2.0 g (25 mmol) CuO to 80 mL of 1 M HCl solution. After that, Solution B in a flat-bottomed flask was ultrasonicated for 15 min, then placed in an ice bath, and 2.33 g (25 mmol) of ANI was added slowly under vigorous stirring. Solution A was added dropwise (approximately one drop/second) into solution B, and the reaction vessel was maintained by continuous stirring for another 24 h at room temperature. Finally, the precipitated composite was filtered, and washed with distilled water until the colorless filtrate was obtained, followed by drying in an air oven at 80 °C for 24 h.

2.3. Characterization of PANI, CuO and PANI-CuO composites

FTIR-ATR spectra were recorded with 32 scans at a resolution of 4 cm^{-1} in the spectral range of 4000–500 cm^{-1} using a Thermo Scientific Nicolet 6700 Spectrometer. Dispersive Raman spectroscopic measurements were performed on a Thermo Scientific DXR Raman Microscope with an accumulation of five scans of 2 s per scan and a resolution of 2 cm^{-1}. All specimens were excited using an Ar^{+} laser power of 10 mW at λ = 532 nm. XRD data were recorded on a Rigaku-D/MAX-Ultima diffractometer (40 kV and 40 mA) in the range of 5-80° with a scanning rate of 2° min^{-1} using Cu Kα radiation ($\lambda = 1.54$ Å). Crystallite sizes (D, nm) of CuO and PANI-CuO composites were calculated using the Scherrer equation (Eq. (1)) related to (−1 1 1) and (1 1 1) reflection planes of CuO [69].

$$D = K\lambda/(\beta cos\theta) \quad (1)$$

where,
K: 0.9
λ: X-ray wavelength (1.5418 Å),
θ: Bragg angle, and.
β: full width at half maximum intensity (FWHM, radians).

SEM analysis was performed on FEI-Philips XL30 Environmental Scanning Electron Microscope with an accelerating voltage of 10 kV. BET measurements were carried out at 77 K using a Quantachrome Quadrosorb SI instrument. Thermal analysis was carried out using a simultaneous TG-DSC instrument (PerkinElmer model STA 600) under an inert pure N_2 atmosphere with a flow rate of 20 mL/min and a heating rate of 10 °C/min.

2.4. Photocatalytic activity experiments

The photocatalytic activity of CuO nanoparticles and three different PCS composites followed by the degradation of RO-122 dye solution (10 mg/L) in the exposure time interval (t = 0–300 min). In an experimental setup, 0.25 mg/L photocatalyst was dispersed in 50 mL of dye solution. The suspension was kept in a cylindrical Pyrex container illuminated from the top with a 125 W black light fluorescent lamp (wavelength range 300–420 nm with a λ_{max} = 365 nm). Then, the suspension was filtered through a 0.22 μm membrane filter (Millipore) at certain time intervals, followed by UV–vis analysis using a Thermo Scientific Genesys 10S double-beam UV–vis spectrophotometer. The maximum wavelength of RO-122 was λ = 484 nm and the percent removal of dye was calculated using Eq. (2).

$$Decolorization, \% = \left((A_o - A)/A_{,o}\right) x100 Rate(R) = -dA/dt = kA \quad (2)$$

where,
A_o: initial absorbance of RO-122.
A_t: absorbance of RO-122 at time t.

2.5. Computational details

The calculations between RR-122 dye and photogenerated hydroxyl radicals were implemented in the Gaussian09 package [70] using the B3LYP/6-31G(d) basis set [71,72]. The CDFT-based reactivity descriptors such as electronic chemical potential, hardness, softness, and Fukui function provide information on the regioselectivity and the reactivity of the compound under investigation. Among them, Fukui function f(r) has an essential role in determining the reactivity site of the molecule [73]. Further details are presented in Supplementary Material (SM) in Part I.

3. Results and Discussion

3.1. FTIR analysis

FTIR spectra of PANI, PCS, and PCI composites are shown in Fig. 1. The characteristic peaks of PANI were located at 1585 cm^{-1} and 1481 cm^{-1} for the C=N and C=C stretching modes of the quinonoid and benzenoid rings, respectively [74]. The medium peak at 1296 cm^{-1} corresponded to the C-N stretching vibration of the aromatic amine

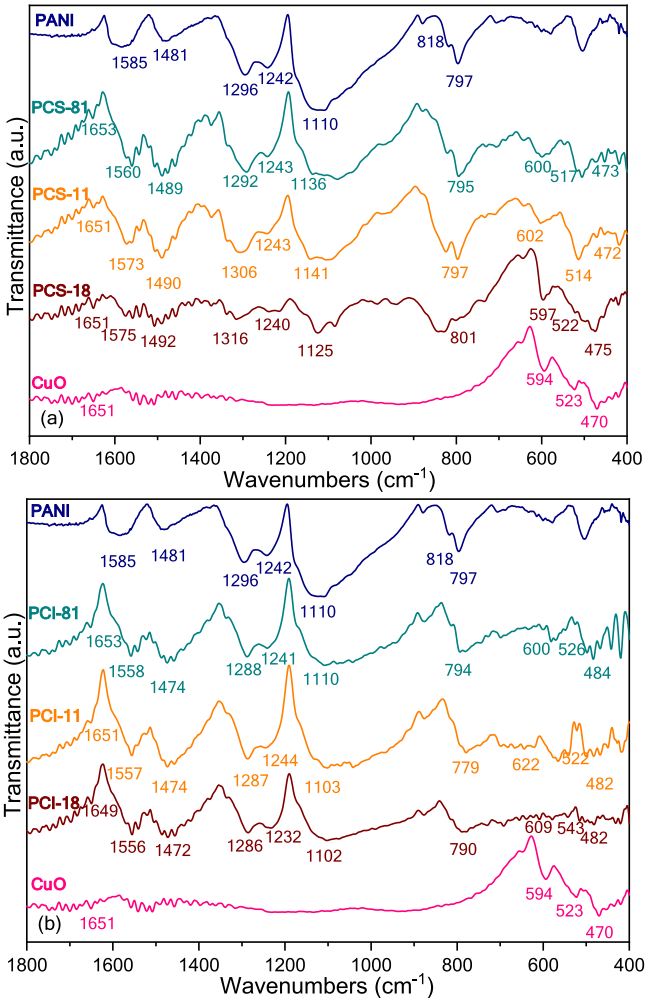

Fig. 1. FTIR spectra of (a) PANI, CuO, and PCS-composites, (b) PANI, CuO, and PCI-composites.

structure. This peak was related to an induced π-electron delocalization in polymer by protonation. Besides, forming a positive charge on the polymer chain (=N^+–H–structure) in strongly acidic media could result in a strong increase in the molecular dipole moment. The peak at 1242 cm^{-1} was attributed to the conducting protonated form of the polymer indicating the presence of C–$N^{+\bullet}$ stretching vibration in the polaron structure. The strong peak at 1110 cm^{-1} could be attributed to a vibrational mode of either B–NH^+=Q or B–$NH^{+\bullet}$–B (B: benzenoid, Q: quinone) charged units formed during the protonation process. This situation also implied the presence of positive charges in the polymer chain and the dihedral angle distribution between the quinone and benzenoid rings [75,76]. The peaks in the 900 cm^{-1}-700 cm^{-1} region (at 818 cm^{-1} and 797 cm^{-1}) belonged to the aromatic-ring and out-of-plane C–H deformation vibrations [77]. The observed peak at 797 cm^{-1} was associated with the C–H out-of-plane bending vibrations on 1,4-substituted benzene rings that indicated the domination of *para*-coupling of constitutional units in PANI chains [75]. The observed bands in FTIR spectrum confirm that the synthesized polyaniline is in the form of emeraldine salt.

For comparison, FTIR spectra of CuO nanoparticles were presented in Fig. 1(a) and Fig. (b). The three characteristic peaks of monoclinic CuO observed at 594 cm^{-1}, 523 cm^{-1}, and 470 cm^{-1} were attributed to the stretching vibrations of the metal–oxygen (Cu–O) bond. FTIR spectrum of CuO exhibited a weak peak at 1651 cm^{-1} corresponding to the bending vibration (O–H group) of absorbed water on the surface [78].

FTIR spectra of PCS-PANI composites revealed the main characteristic peaks of both PANI and CuO (Fig. 1(a)). The peaks corresponding to quinonoid and benzenoid rings of PANI at 1585 cm^{-1} and 1481 cm^{-1} shifted to 1560 cm^{-1} and 1489 cm^{-1} in the spectrum of PCS-81 composite, respectively. The observed remarkable blue shift of benzenoid ring vibration in PCS-81 could indicate the presence of an electrostatic interaction between a charged structure of PANI and CuO nanoparticles [56]. Depending on the increased amount of CuO in PCS-PANI composites, quinonoid and benzenoid ring peaks representing the backbone of PANI shifted to higher wavenumbers, and their intensities also decreased gradually. For PCS-81, the peaks at 1292 cm^{-1}, 1243 cm^{-1}, 1136 cm^{-1}, 795 cm^{-1}, and 506 cm^{-1} were related to PANI while the peaks observed at 600 cm^{-1}, 517 cm^{-1}, and 473 cm^{-1} corresponded to CuO. The spectrum of PCS-11 composite was almost identical to that of PCS-81 although the peaks were generally shifted towards a higher frequency side. However, PCI composites presented only the characteristic vibrations belonging to PANI that differed or changed in peak locations and intensities (Fig. 1(b)). As clearly seen in the FTIR spectra, all PCI composites are quite similar and have mostly PANI signals with no indication of the presence of CuO. Although there are reports available on the preparation of PANI-CuO composites using HCl [54,56–58], they all seem to be skeptical in this regard due to the fact that CuO is not stable in an acidic environment [79]. This result is also in agreement with the yields obtained during the preparation of the composites. Even for the PCI 18 composite with the highest CuO content, the yield obtained after the preparation attempt was found to be significantly lower and this yield corresponds to the PANI ratio that should theoretically be present in the composite. Thus, the phenomenon is attributed to the dissolution of CuO and releasing Cu^{2+} ions under acidic conditions [79].

3.2. Raman analysis

Raman spectroscopy was used to determine the compositional and structural features of PANI, PCS, and PCI composites (SM, Part II, in Fig. S1). PANI exhibited two wide bands at 1567 cm^{-1} and 1345 cm^{-1} corresponding to the C=C ring stretching of quinonoid and C–$N^{+\bullet}$ stretching in polaronic form, respectively. The presence of this radical cation could indicate the conversion of quinonoid rings to benzenoid rings [80,81].

The band related to the C=C stretching vibration of the quinonoid ring in the PCS-81 composite shifted to 1588 cm^{-1}. This upward shift in the spectral position was also observed in PCS-11 and PCS-18 composites compared to PANI. In the PCS-81 spectrum, the shifted band observed at 1328 cm^{-1} was linked to the C–$N^{+\bullet}$ vibration. As the CuO amount increased, this band shifted to lower values (1327 cm^{-1} and 1310 cm^{-1}), and the intensity of the bands decreased. In the case of PCS-81, the observed bands at 1605 cm^{-1}, 1470 cm^{-1}, 1213 cm^{-1}, 1164 cm^{-1}, and 785 cm^{-1} corresponded to the C − C stretching in the benzenoid ring, C=N stretching in the quinonoid unit, C − N stretching vibrations, C − H bending vibration, and benzene ring deformations, respectively. The other bands at 660 cm^{-1}, 588 cm^{-1}, 514 cm^{-1}, and 422 cm^{-1} were attributed to the C − H vibrations in the quinonoid unit [82,83]. The presence of the Cu − O vibration at 639 cm^{-1} confirmed the monoclinic CuO [84]. This weak band observed for PCS composites could not be distinguished in the spectra of PCI composites. The bands observed at Raman spectra of PCS-11 and PCS-18 composites were similar to those of PCS-81 composite with shifts from original positions. Raman spectra of PCI composites presented PANI bands and confirmed FTIR results.

3.3. XRD analysis

The structural properties of PANI, CuO, PCS-PANI, and PCI-PANI composites were investigated via XRD analysis (Fig. 2). The observed semi-crystalline peaks of PANI at 2θ = 8.99°, 15.42°, 20.34°, 25.30°, and 27.18° could be indexed to the (0 0 1), (0 1 1), (0 2 0), (2 0 0), and (1 2 1) reflection planes, respectively [85]. The XRD diffractogram of CuO revealed two intense peaks located at 2θ = 35.56° and 38.72° were the characteristic monoclinic (−1 1 1) and (1 1 1) planes of the CuO phase, respectively. The other diffraction peaks were observed at 2θ = 32.54°, 48.80°, 53.36°, 58.32°, 61.56°, 65.84°, 66.30°, 68.12°, 72.44°, and 75.02° corresponded to (1 1 0), (−2 0 2), (0 2 0), (2 0 2), (−1 1 3), (0 2 2), (−3 1 1), (2 2 0), (3 1 1) and (0 0 4) planes of monoclinic CuO crystals following the standard (JCPDS card no. 89–5895) [86].

The XRD diffractograms of PCS-PANI composites are presented in Fig. 2(a). The diffractogram of the PCS-81 composite highlighted semicrystalline peaks of PANI at 2θ = 8.93°, 15.28°, 20.46°, 25.04°, and 26.85° corresponding to (0 0 1), (0 1 1), (0 2 0), (2 0 0), and (1 2 1) planes. Conversely, the observed peaks at 2θ = 32.18°, 35.46°, 38.64°, 48.69°, 53.51°, 58.36°, 61.52°, 65.49°, 66.24°, 68.19°, and 72.19° attributed to (1 1 0), (−1 1 1), (1 1 1), (−2 0 2), (0 2 0), (2 0 2), (−1 1 3), (0 2 2), (−3 1 1), (2 2 0), and (3 1 1) planes of monoclinic CuO crystals and these high-intensity characteristic peaks were also decreased substantially due to the domination of PANI peaks over CuO. The XRD pattern of PCS-11 revealed a pattern consisting of the typical diffraction peaks of CuO and PANI. However, with a further increase in CuO, three reduced diffraction planes of PANI assigned to (0 1 1), (0 2 0), and (2 0 0) were present in PCS-11, and then all PANI planes disappeared in the PCS-18 composite. The total amount of PANI in the PCS-18 composite could be below the detection limit of XRD and also the adsorption layer of PANI chains on the CuO surface [87]. XRD diffractograms of PCI-PANI composites displayed reflections corresponding to PANI whereas the characteristic reflections associated with CuO were absent (Fig. 2(b)). The reason is the dissolution of CuO in a highly acidic medium during synthesis and this result complemented FTIR and Raman characterization.

The spectral shift observed for the dominant peaks of CuO located at 2θ = 35.56° and 38.72° associated with (−1 1 1) and (1 1 1) planes were represented in Fig. 2(c). These two major diffraction peaks slightly shifted towards a lower diffraction angle (left side) in PCS-PANI composites indicating the interactions between the PANI chain and CuO [56]. Similarly, the intensities and related peak positions were gradually altered with the increase in PANI amount. The values of crystallite sizes using the Scherrer equation by measuring diffraction planes (−1 1 1) and (1 1 1) of CuO were presented in SM in Part II, Table S1. The crystallite sizes of the PCS composites decreased with increased CuO amount. The calculated crystallite sizes of PCS composites were higher

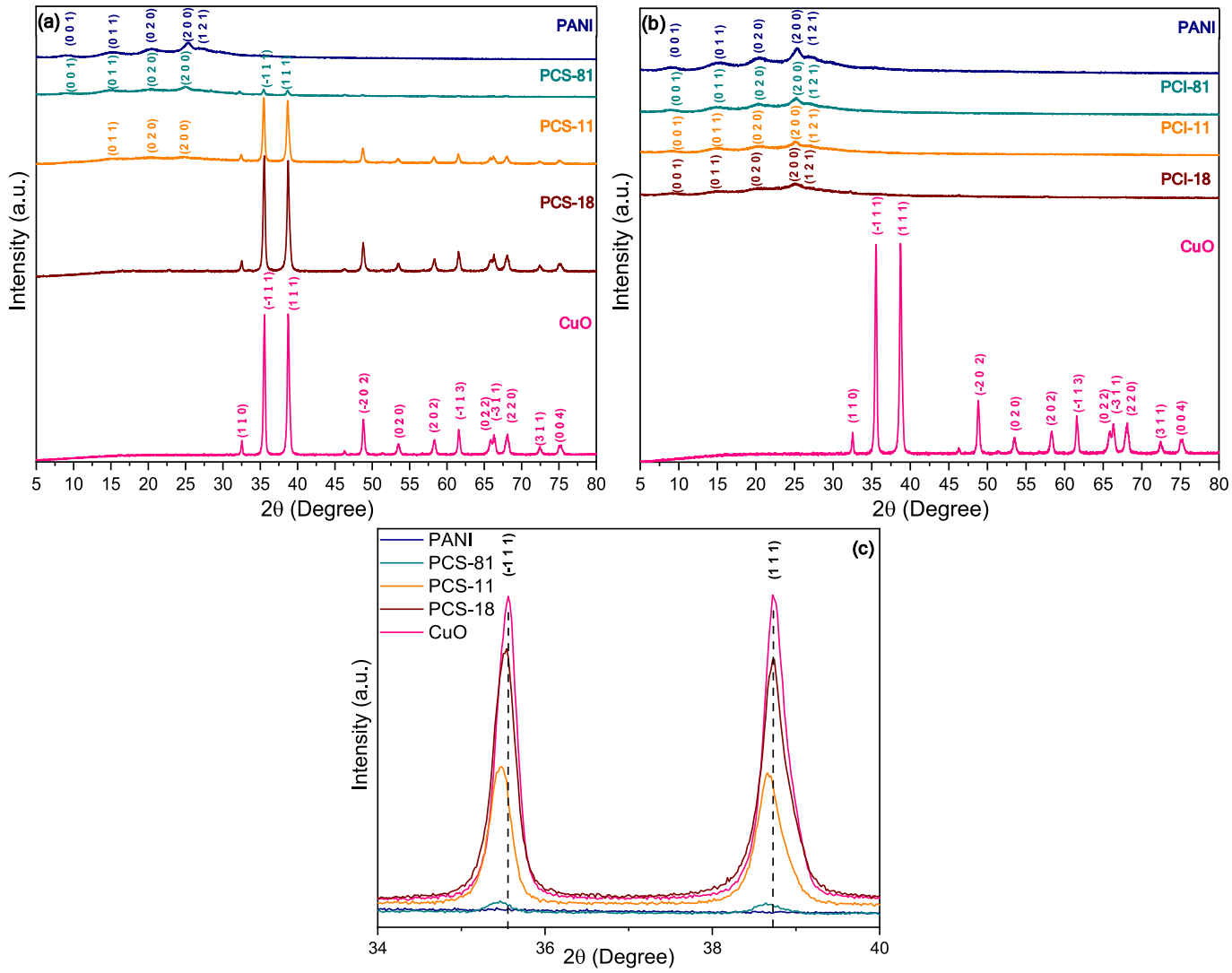

Fig. 2. XRD diffractograms for (a) PANI, PCS-PANI composites, and CuO, (b) PANI, PCI-PANI composites, and CuO, and (c) XRD peaks for (−1 1 1) and (1 1 1) planes of PANI, CuO, and PCS-PANI composites.

than the values reported previously [88]. Verma et al. found that the crystallite sizes of PANI-CuO composites ranged from 12.2 nm to 17.8 nm, and the crystallite sizes of composites increased with higher concentrations of CuO [88]. In another study, the crystallite size of the PANI-CuO composite was found to be 58.8 nm, which was higher than the result we obtained [89].

3.4. SEM analysis

The surface morphology of PANI, CuO, PCS-PANI, and PCI-PANI composites was analyzed, and the corresponding SEM images at a magnification of (x100000) were shown in Fig. 3.

SEM images of PANI (Fig. 3(a)) revealed a large globule-structured shape while CuO particles (Fig. 3(e)) were closely packed in various polyhedral-shaped structures. SEM image corresponded to PCS-81 (Fig. 3(b)), wherein CuO particles were slightly arranged and stacked in a high PANI content composite, i.e. no significant change was observed in the features of the PANI in composite morphology even at higher magnifications. SEM image of PCS-11 maintained the morphology of the two components within an overlapped matrix and particles were slightly arranged and stacked (Fig. 3(c)). However, the PCS-18 composite (Fig. 3(d)) comprised a binary-type structure containing polyhedral-shaped CuO and flakes-like aggregated particles. The globule particles of PANI were no longer observed significantly due to the dominant morphology of CuO covering the porous structure of PANI. As the amount of CuO in PCS composites increased, the size of the agglomerated particles also enhanced due to a higher tendency for agglomeration.SEM images of PCI composites having different CuO amounts were presented in Fig. 3(f–h). It was noticeable that the surface morphologies of PCI-81 (Fig. 3(f)) and PCI-11 (Fig. 3(g)) composites were similar to the typical PANI matrix with a more loosely packed structure as compared to PCS composites. The particle sizes of the PCI-81 and PCI-11 composites were nearly identical. Indeed, an increase in CuO amount affected polymer morphology remarkably in the PCI-18 composite (Fig. 3(h)), and surface modification resulted in a lose cotton-like structure as reported in literature [90]. The reason could be the alteration in coordination geometry of transition metal ion Cu^{2+} derived from the dissolution of CuO [91]. SEM results were consistent with the previously discussed spectroscopic data regarding the issue of CuO dissolution in highly acidic conditions.

3.5. BET analysis

Nitrogen adsorption–desorption isotherms of PANI, CuO, PCS, and PCI composites are presented in SM, Part II, in Fig. S2 and Fig. S3. All isotherms and hysteresis curves were recognized according to the

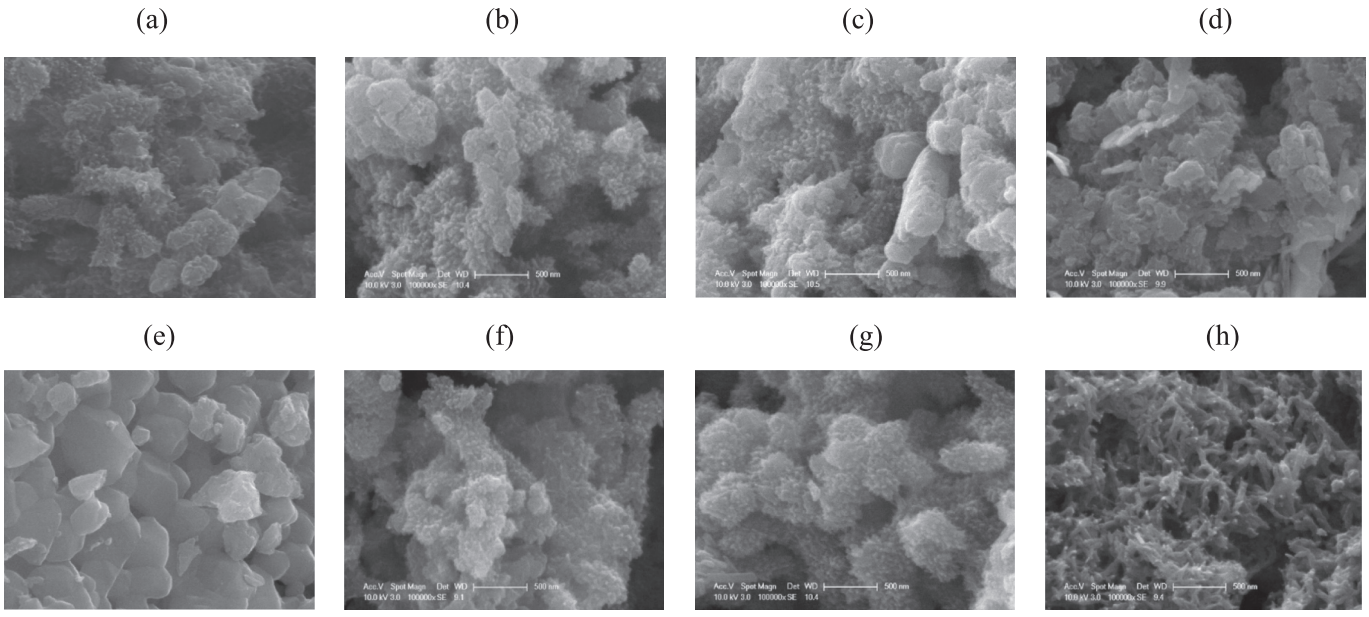

Fig. 3. SEM images (x100000) of (a) PANI, (b) PCS-81, (c) PCS-11, (d) PCS-18, (e) CuO, (f) PCI-81, (g) PCI-11, and (h) PCI-18.

International Union of Pure and Applied Chemistry (IUPAC) classification [92]. PANI isotherm curve belonged to type III, indicating weak interaction with the adsorbate at high pressure (P/P_o), as reported by other researchers [93–95]. The isotherms of CuO, PCS, and PCI composites revealed a type IV curve trend. CuO was attributed to a H3 loop indicating aggregates of plate-like particles whereas an H4 loop was observed on PCS and PCI composites and could be related to narrow slit pores [96].

The BET surface parameters of PANI, CuO, PCS, and PCI composites are listed in SM, Part II, Table S2. The surface area of PANI was 26 m^2/g and this value closely agreed with the recently reported study [93,94]. The specific surface area of CuO (3 m^2/g) was increased after PANI matrix formation in PCS composites. PCS-81 composite as the main constituent of the PANI amount exhibited the highest specific surface area (32 m^2/g) in PCS composites. It could be seen that the surface area of the PCS-81 composite increased to about 11 times compared with CuO. A remarkable enhancement was also observed on the surface area of PCS-11 (20 m^2/g) compared to CuO while the surface area of PCS-18

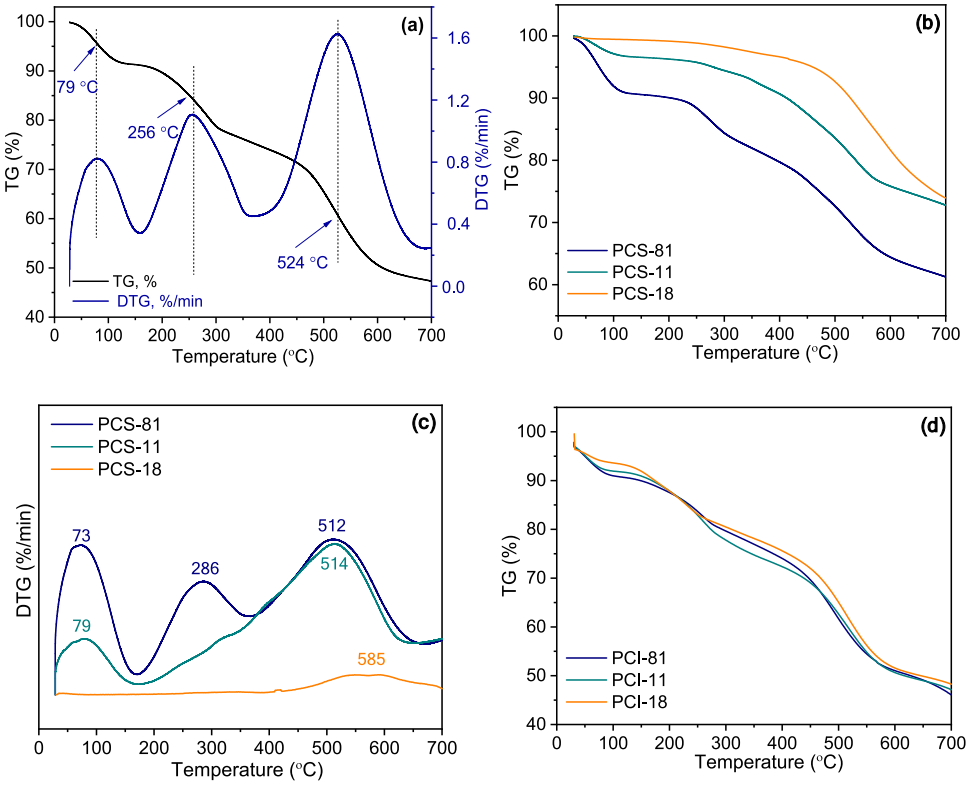

Fig. 4. (a) TG and DTG curves of PANI, (b) TG and (c) DTG curves of PCS composites, and (d) TG curves of PCI composites.

(5 m^2/g) composite containing the highest CuO content was slightly altered. In addition, the pore size and pore volume of CuO were also increased after surface modification with PANI. The porous feature of the obtained results was consistent with SEM analysis. The average pore sizes of PCS composites were fitted with the mesoporous range of the IUPAC [92].

The surface areas of PCI-81 (28 m^2/g) and PCI-11 (27 m^2/g) composites were close to PANI (26 m^2/g). However, the surface area of the PCI-18 composite was obtained as 45 m^2/g, much higher than that of the CuO specimen (3 m^2/g). This result could also be confirmed by the cotton-like structure of the composite, also seen in the SEM image (Fig. 3 (h)). Accordingly, adding CuO affected the surface morphological properties and surface areas of PCI composites.

3.6. Thermogravimetric analysis

TGA analysis was carried out to investigate the thermal behavior of PANI and PCS composites (Fig. 4). The thermal decomposition of PANI revealed four main continuous weight loss steps with temperature, as presented in Fig. 4(a). In general, the weight loss was observed at a temperature up to 120 °C corresponding to the evaporation of water molecules in PANI chains and the elimination of the unreacted aniline monomer, if left. A small drop in weight loss at around 80 °C was only 4.4 % and was associated with the release of water. The second step was observed at the temperature range between 165 °C to 360 °C related to the loss of impurities, small-chain oligomers and/or dopants. The observed endothermic peak was at around 256 °C and the total weight loss was 15.6 %. A sharp weight loss between 405 °C and 675 °C was associated with the thermal decomposition of PANI chains and the polymeric backbone. This significant additional weight loss was 23.3 % as the temperature reached 524 °C. An initial stage of PANI carbonization could be found under a nitrogen atmosphere around 700 °C and PANI lost its total weight of 52.7 % [47,97].

TG and DTG curve profiles of PCS composites were presented in Fig. 4((b)-(c)). PCS-81 composite exhibited a similar thermal decomposition pattern as PANI. The initial peak at around 73 °C corresponded to the moisture, and the endothermal peak at 286 °C reflected the loss of dopant molecules inside the PANI-CuO composite matrix. The decomposition of the polymer matrix in PCS-81 was characterized at a temperature of 512 °C. However, the increase in CuO amount in PCS composites revealed a higher residue formation and a shift towards a higher decomposition temperature. Total weight losses were 52.7 %, 38.75, 27.22 %, and 26.06 % for PANI, PCS-81, PCS-11, and PCS-18, respectively. A wide degradation curve belonging to the decomposition of the skeletal polymer was monitored from 200 °C and ended at 650 °C in PCS-11 composite whereas, the main decrement in the thermal decomposition of PCS-81 was observed around 585 °C and continued until 700 °C. The TG profiles of each PCI composite were almost the same and these three composites exhibited similar thermal behavior of PANI (Fig. 4((d)). The total weight losses of PCI composites were the same as PANI (~53 %), which is a strong indication of the dissolution issue of CuO in a highly acidic medium.

3.7. PL analysis

Photoluminescence spectra of CuO and PCS composites are shown in SM, Part II, in Fig. S4. The PL spectrum of CuO revealed a strong visible band at 411 nm (3.02 eV) corresponding to the edge of CuO [98]. The combination of CuO with PANI resulted in a significant reduction in the intensity of PL bands and shifts in peak positions towards 406 nm (3.05 eV), 408 nm (3.04 eV), and 409 nm (3.03 eV) were recorded for PCS-18, PCS-11, and PCS-81, respectively. The broad green band at 524 nm (2.37 eV) could have originated from the ionized oxygen vacancies, and the wavelength was in the range of 511 nm-520 nm in PCS composites [86].

3.8. Photocatalytic activity

3.8.1. Photocatalytic degradation of RO-122

The changes in UV–vis spectra of RO-122 were investigated using CuO particles and PCS composites and presented in Fig. 5. The spectrum of RO-122 revealed a maximum absorption band at $\lambda_{max} = 484$ nm with a shoulder at $\lambda = 404$ nm [12]. The bands at 226 nm and 270 nm could be related to the aromatic groups [99]. A gradual decrease in the intensity of the maximum absorption bands at $\lambda = 484$ nm was observed with increasing reaction time. The destruction of the main band in the visible region of RO-122 in the presence of PCS-81 composite confirmed an almost complete photocatalytic degradation of RO-122 dye in 120 min. This could be evidence of the chromophore containing the breakage of the azo bond (Fig. 5(a)). A similar gradual disappearance occurred in UV bands corresponding to the aromatic groups of RO-122 in solution in the presence of PCS-81. An almost complete disappearance of the maximum absorption band of the RO-122 dye was observed after 300 min of using the PCS-11 composite. However, a much slower gradual decreasing trend in characteristic band intensities was observed in the case of the PCS-18 and CuO specimens.

The photocatalytic performance of CuO particles and PCS composites on RO-122 was analyzed at different time intervals (Fig. S5), and related data was reported in SI, Part III, Table S3. The pH_{pzc} values of PANI and CuO were $pH_{pzc} = 7.3$ and $pH_{pzc} = \sim 8.5$, respectively [100,101]. Since RO-122 as an anionic dye was negatively charged, the attractive electrostatic interactions between the dye and PCS composites could result in an efficient degradation. Upon comparing PCS composites, the highest removal percentage of RO-122 degradation achieved in PCS-81 in 120 min was 91 %. The logarithmic decay profiles of RO-122 using CuO nanoparticles and PCS composites obeyed the pseudo-first-order kinetics model (SI, Part III, Fig. S6). The kinetic model parameters ($R^2 > 0.75$) were calculated by Eq. (3) and presented in Table 1.

$$Rate(R) = -dA/dt = kA \quad (3)$$

where,

R: pseudo-first-order rate ($cm^{-1}min^{-1}$),

A_o: initial absorbance of dye,

A: absorbance of dye at time t,

t: irradiation time, min,

k: pseudo first-order reaction rate constant, min^{-1}.

Half-life ($t_{1/2}$, min) could easily be calculated by the following equation, $t_{1/2} = 0.692/k$.

Upon use of all specimens, the trend in photocatalytic degradation rate constants could be presented in decreasing order:

PCS-81 > PCS-11 > PCS-18 > CuO.

The PCS-81 composite revealed the fastest rate constant, whereas the CuO exhibited the lowest decolorization rate constant in the case of all specimens. Accordingly, the high BET surface area (Table S2) and considerable surface hydroxyl groups, as evidenced by FTIR (Fig. 1(b)) could be the basis of the high photocatalytic efficiency. It was well known that the number of surface hydroxyl groups could affect the adsorption of organic pollutants and lead to an enhancement in photocatalytic activity [102]. This result could be confirmed by the surface coverage values of PCS-81 (23 %) and CuO (4 %) specimens in Table S3 and Fig. S5.

3.9. Reusability and recyclability

The reusability and structural stability of the PCS-11 composite were tested for four consecutive cycles of degradation of RO-122 azo dye (10 mg/L). The recyclability of PCS-11 composite (0.25 g/L) was studied under the same experimental conditions in 60 min irradiation. Following each treatment, the used composite was removed from the dye solution by centrifugation, washed with distilled water, and dried at 80 °C for the next run. To clarify the structural and morphological

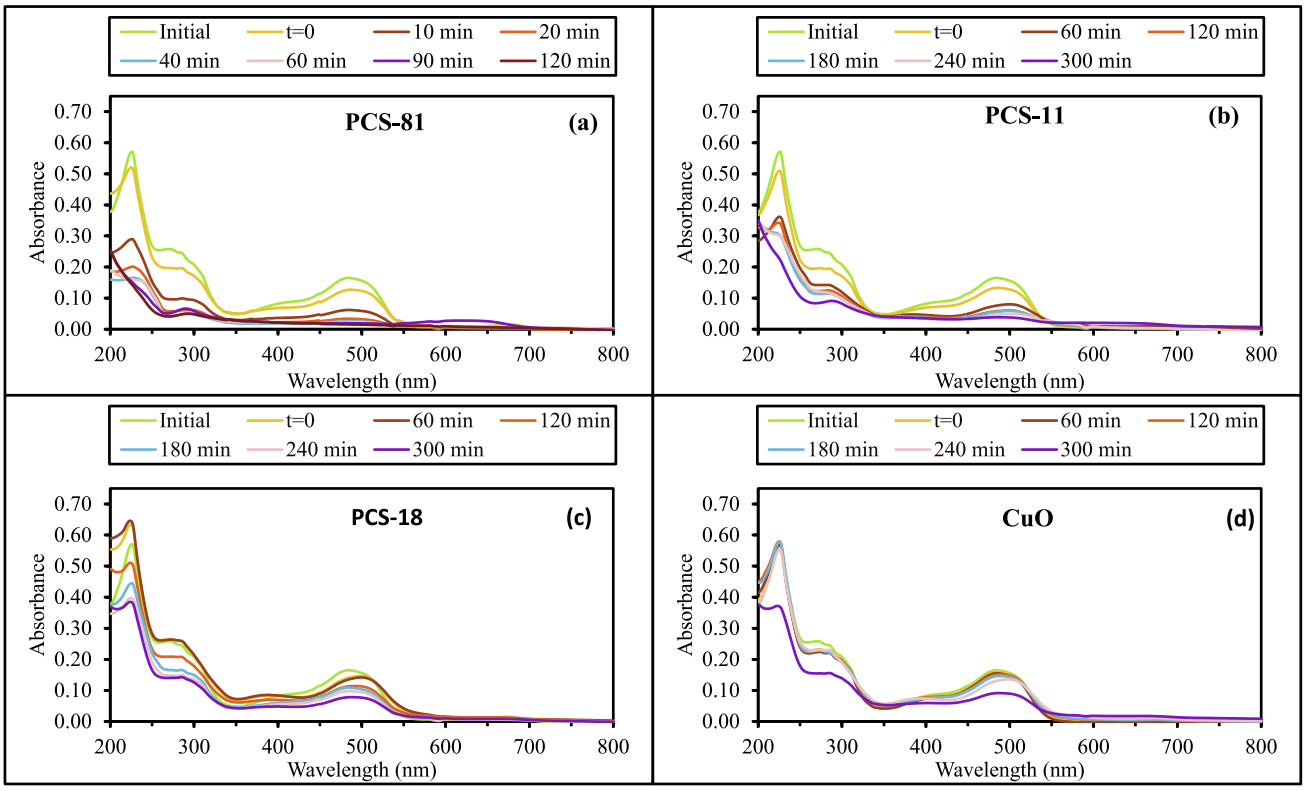

Fig. 5. UV–vis absorption spectra of RO-122 using (a) PCS-81, (b) PCS-11, (c) PCS-18, and (d) CuO.

Table 1
Photocatalytic degradation kinetics of RO-122 upon use of CuO particles and PCS composites.

Specimens	First-order kinetic parameters kx10^{-3}, min^{-1}	$t_{1/2}$, min	Rate, cm^{-1} min^{-1}
CuO	1.67	415	0.00028
PCS-18	2.26	307	0.00037
PCS-11	4.21	165	0.00069
PCS-81	15.6	45	0.00257

changes of PCS-11 after four consecutive cycles were further characterized.

The removal performance of recycled and reused PCS-11 composite for four cycles was almost maintained as efficiently as the initial cycle (Fig. S7). The photocatalytic degradation of RO-122 for three cycles is 54 %, 49 %, and 48 %, respectively. At the end of the last cycle, the activity of the PCS-11 composite dropped further to 41 % removal of RO-122, and the conversion efficiency obtained was still 76 % at the fourth cycle. A slight decline in photocatalytic activity after each run could be related to the minor photocatalyst dose. The reason could be the deactivation of active sites and aggregation caused by the subsequent heat process [103].

FTIR spectra of the PCS-11 composite before and after different cycles are displayed in Fig. S8. The spectrum adsorbed RO-122 dye on PCS-11 (referred to as, t = 0) was almost similar in shape and position to that of the sole PCS-11. In addition, an obvious change was not observed in the FTIR recycled spectra during repeated photocatalytic processes suggesting a stable catalyst.

In order to expand the structural evaluation of the usability of the PCS-11 composite, XRD analysis was carried out. XRD diffractograms of the unused and used PCS-11 composites were investigated to evaluate the possible differences in crystalline structure (Fig. S9). In comparison with the XRD diffractogram of the PCS-11 composite, that of the adsorbed RO-122 dye on the catalyst surface (t = 0) slightly changed and the minor peaks corresponding to the (0 1 1) and (2 0 0) planes of PANI disappeared. After four consecutive cycles, the intensities of the diffraction peaks of CuO decreased slightly due to the adsorption of RO-122 on PCS-11. Through recycling processes, XRD diffractograms of PCS-11 composite almost preserved the characteristic diffraction peaks of the composite and maintained crystalline structure with a minor alteration.

The morphology of the unused and reused PCS-11 composite at the end of each cycle was investigated by SEM images presented in Fig. S10. For comparative purposes, the SEM image of the PCS-11 composite was presented in Fig. 3(c) in the previous data set, referred to here as Fig. S10 (a). After the adsorption of RO-122 on PCS-11 (t = 0), a decrease in surface roughness was observed (Fig. S10 (b)). The influence of the recovery and recycling process on morphology did not exhibit a significant difference compared with that of unused PCS-11. The particles were mostly similar in shape and size to PCS-11, whereas a slight aggregation was observed after the 4th cycle process (Fig. S10(c)-(f)).

In general, FTIR and Raman spectra of repeated four cycles of PCS-11 revealed an insignificant shift in peak positions on the functional groups confirming the structural properties of the composite almost remain unchanged. SEM images indicated minimal surface morphology changes during the recycling process, although a slight agglomeration was observed in the 4th cycle. The agglomeration observed in the 4th cycle, thus leading to a decrease in surface area, is also consistent with the sudden decrease in the removal efficiency of the composite. A minor alteration was observed in the crystalline structure of the PCS-11 composite after cyclic use. These outcomes indicated remarkable stability and reusability of PCS-11 composite as a catalyst in the future.

3.10. Degradation mechanism of RO-122

The optimum geometric structure of RO-122 was displayed in SI, Part IV, Fig. S11. The possible degradation mechanism of RO-122 upon PCS-11 composite was proposed using Fukui functions and further

detailed characterization of the progress of the photodegradation process was performed via FTIR and SEM analysis.

3.10.1. FTIR analysis

FTIR analysis was used to monitor the structural changes of functional groups during photocatalytic degradation of RO-122 with different time intervals (Fig. S12). Previous experimental FTIR data of PCS-11 and adsorption of RO-122 on PC-11 (t = 0) were given in Fig. S8, respectively for comparative purposes (referred to Fig. S12).

In the FTIR spectrum of RO-122 adsorption on PCS-11 (t = 0), peak positions and intensities were slightly changed compared to PCS-11. The observed peaks at 1575 cm^{-1}, 1491 cm^{-1}, 1306 cm^{-1}, 1244 cm^{-1}, 1143 cm^{-1}, 798 cm^{-1}, and corresponded to PANI while the peaks at 599 cm^{-1}, 512 cm^{-1}, and 461 cm^{-1} were attributed to CuO. In addition, the appeared peak at 1636 cm^{-1} could be the combination of phenyl ring vibrations with the stretching of the C=N group of dye [104]. Accordingly, the presence of novel peaks could indicate further evidence of the electrostatic interaction between the negative charge on the surface of RO-122 and the positive charge of the PCS-11 composite from the driving forces of adsorption [105].

The progress of the photocatalytic reaction was also followed at different irradiation times and FTIR spectra of RO-122 revealed changes in peak intensities and positions. The observed peak at 1491 cm^{-1} corresponded to the − N=N − bond stretching of dye or the characteristic peak of PANI vibration. However, the intensity of the chromophore group of RO-122 at 60 min irradiation decreased gradually as the reaction time increased. The presence of the azo bond even after 300 min of irradiation could indicate an incomplete decolorization and was compatible with the UV degradation profile presented in Fig. 5 (b) and Fig. S5.

3.10.2. SEM analysis

The morphological changes before and after the photocatalytic process at different irradiation times were investigated by SEM analysis. The previously presented SEM images of PCS-11 (Fig. S10 (a)) and t = 0 (Fig. S10 (b)) were referred to here as Fig. S13 (a)-(b) respectively. After 60 min photocatalytic degradation, the morphology was similar to that of untreated PCS-11 composite (Fig. S13 (c)). As irradiation time increased to 120 min, the SEM image revealed large globular-shaped PANI particles and polyhedral-shaped CuO particles with a slight particle agglomeration (Fig. S13(d). Furthermore, a longer irradiation time resulted in a smoother surface and contained more aggregated particles compared to PCS-11 (Fig. S13 (e)).

3.10.3. Theoretical Prediction of degradation mechanism of RO-122

Fukui indices values were calculated to predict the susceptive reactive centers of RO-122 dye vulnerable to hydroxyl radical (•OH) attacks. The local softness s°, Fukui f°, and softness difference, Δs° values are calculated and presented in Table 2. Since the highest f° values were the possible sites for •OH attack, the sites concerned with relatively low Fukui function values were not presented. The selected specific sites of the RO-122 molecule were determined by the softness values being close to that of hydroxyl radical. In orbital-controlled reactions, Δs° values between the reacting atoms should be as small as possible [67]. The numbering system throughout the calculations is presented in Fig. 6.

According to the literature, nitrogen atoms of azo bonds were the primary targets for •OH attack, following the cleavage of N − N and C − N bonds [68,106]. In another computational study, Fukui indices were calculated to address the •OH attack on reactive regions of an azo dye, and the highest f^0 values corresponded to the double azo bond (−N=N −) and single (−NH −) bond [107]. From Table 2, the highest f^0 values belonged to four nitrogen atoms corresponding to N17, N26 N49, and N50 were the most susceptive reactive sites for •OH attack in contrast with others and resulted in fragments (I) and (II). Based on the above experimental results and combining calculated computational parameters and relevant literature, two main competing possible photocatalytic degradation pathways of RO-122 were proposed (Fig. 6).

Table 2
Chemical reactivity descriptors for RO-122 and •OH.

RO-122 (S = 7.29065)	f°	s°	Δs°
N 17	0.07158	0.58536	3.85348
N 26	0.06251	0.48123	3.92590
N 49	0.06337	0.49453	3.99523
Cl 25	0.04523	0.35523	4.12357
N 50	0.05863	0.48523	4.15263
C 51	0.02885	0.22519	4.18832
S 39	0.02382	0.17652	4.23562
S 44	0.02412	0.17547	4.23689
S 66	0.02417	0.17863	4.23987
O 67	0.02412	0.16782	4.24213
O 45	0.02125	0.16478	4.24366
S 71	0.02569	0.18124	4.24623
O 38	0.02325	0.16521	4.24689
O 69	0.02225	0.16325	4.24789
O 72	0.02396	0.16933	4.24814
O 40	0.02092	0.16328	4.25023
O 74	0.02325	0.17426	4.25236
O 75	0.02236	0.17423	4.25258
O 41	0.02025	0.15807	4.25545
O 47	0.02177	0.15987	4.25652
O 70	0.02136	0.16458	4.26523
O 42	0.01892	0.14748	4.26608
O 48	0.01963	0.15410	4.27523
H 73	0.00823	0.06412	4.31236
C 13	0.00682	0.05512	4.32356
H 18	0.00923	0.07032	4.34228
C 20	0.00825	0.06442	4.34908
H 68	0.00814	0.06352	4.34999
H 27	0.00687	0.05392	4.36210
C 19	0.00662	0.05236	4.36256
•OH (S = 5.71430)			

Pathway I: The most plausible site for •OH attack was the position on the N17 atom with the highest f^0. The cleavage of the − N17H- bond between the naphthalene ring and triazine group resulted in the compound (1) that proceeded into two possible pathways. In the suggested pathway, the •OH attack to the N26 atom was potentially cleaved to form compounds (2) and (3) and further degraded into smaller molecules by the cleavage of ring structures.

Pathway II: The main structure of this pathway, fragment (II) proceeded to the breakage of the azo bond between N49 and N50 atoms attached to the naphthalene rings, thus yielding a hydroxylated compound (5), followed by the removal of sulfonate groups on the naphthalene ring (6). Similarly, the attack of the •OH on the C51 atom could generate a compound (7), and then the elimination of the SO_3H group to give a compound (8). Finally, hydroxylated compounds (6) and (8) were further ring-opening naphthalene rings that could mineralize into small molecules such as CO_2 and H_2O.

DFT calculations were consistent with UV–vis and FTIR experimental results. A gradual decrease was observed in the aromatic and chromophore groups corresponding to UV and FTIR spectral bands of RO-122 upon PCS-11. However, the high-molecular-weight aromatic ring structures were difficult to eliminate, and an extended irradiation time was needed. The proposed degradation mechanism was mostly compatible with the GC–MS analysis reported in the literature [108]. However, additional complementary analytical spectroscopic techniques were necessary to completely identify the intermediates generated in the mechanism of photocatalytic degradation in the future.

4. Conclusions

PANI-CuO composites were synthesized using two different routes, *in-situ* chemical oxidation polymerization and mechano-chemical preparation methods. The amount of CuO, as well as the synthesis route, played a significant role in determining the morphology, structure,

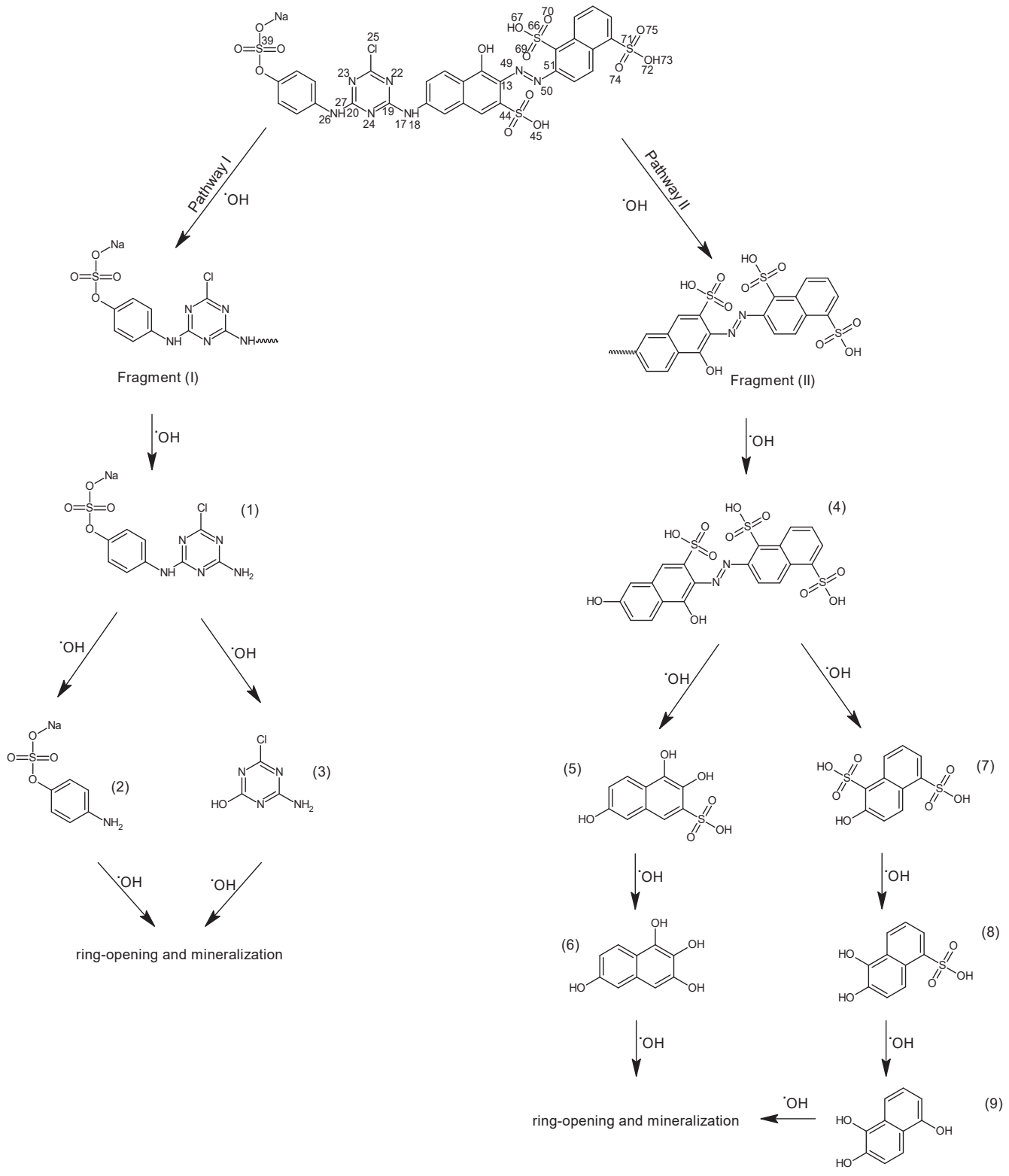

Fig. 6. Proposed photocatalytic degradation mechanism of RO-122.

optical, and surface features of PANI-CuO composites for the design of future catalysts.

The spectroscopic analysis of PCS specimens revealed that the composites almost exhibited the same main functional group vibrations of PANI and CuO with a slight alteration in peak locations and intensities. A systematic improvement in crystallinity with a strong dependency on the amount of CuO was presented in PCS composites. The addition of CuO influenced the morphologies of PCS composites, and these three different amounts of PCS composites exhibited dual morphology from the dominant feature of PANI to the various polyhedral-shaped characteristics of CuO structure. Unlike PCI composites, it was determined that CuO dissolves in acidic medium during the preparation of PCI composites and thus affects the structural, morphological, and thermal properties. The impact of CuO amount

resulted in more alterations in terms of morphologies and surface areas, this fact was obvious in the PCI-18 composite with observed lose cotton-like structural morphology derived from the dissolution of CuO.

The photocatalytic performances of CuO and PCS composites were studied in the degradation of an anionic RO-122 dye. From a general UV–vis spectral perspective, the intensities of characteristic bands belonging to RO-122 in the presence of catalysts decreased gradually. The best photocatalytic performance observed for RO-122 was 91 % in the presence of PCS-81 under 120 min irradiation.

The photocatalytic activity of the PCS-11 composite remained almost stable even after four consecutive cycles. Moreover, FTIR, XRD, Raman, and SEM results confirmed that the structural and morphological stability of the reused PCS-11 composite was maintained. Based on recyclability tests, this catalyst exhibited great potential as a reusable catalyst in the future. However, further experiments in a pilot plant are suggested to evaluate the feasibility of practical applications of PANI-CuO composites.

In the computational part, CFDT was applied on the reactive sites of RO-122 vulnerable to •OH attacks and chemical reactivity descriptors were calculated using the DFT/B3LYP/6-31G(d) theory. A plausible degradation mechanism was predicted using Fukui indices and indicated two main competing possible photocatalytic degradation pathways of RO-122 based on the cleavages of double azo (−N=N −) and single (−NH −) bonds. Moreover, FTIR and SEM analysis were applied to examine the considerable changes in the structure and morphology on the progress of the photodegradation process of RO-122. DFT calculations were consistent with experimental results and relevant literature data.

CRediT authorship contribution statement

Nazli Turkten: Writing – review & editing, Investigation, Formal analysis. **Yunus Karatas:** Writing – review & editing, Supervision, Investigation, Conceptualization. **Yelda Yalcin Gurkan:** Writing – review & editing, Software, Investigation.

Declaration of competing interest

The authors declare that they have no known competing financial interests or personal relationships that could have appeared to influence the work reported in this paper.

Acknowledgments

The financial support provided by Research Fund of Tubitak through Project No. 221Z258 and Tekirdag Namik Kemal University BAP unit through Project No. NKUBAP. 01.GA.22.437 is gratefully acknowledged.

Appendix A. Supplementary data

Supplementary data to this article can be found online at https://doi.org/10.1016/j.inoche.2025.113919.

Data availability

Data will be made available on request.

References

[1] S.H. Teo, C.H. Ng, A. Islam, G. Abdulkareem-Alsultan, C.G. Joseph, J. Janaun, Y. H. Taufiq-Yap, S. Khandaker, G.J. Islam, H. Znad, M.R. Awual, Sustainable toxic dyes removal with advanced materials for clean water production: A comprehensive review, J. Clean. Prod. 332 (2022) 130039.

[2] M.D. Khan, A. Singh, M.Z. Khan, S. Tabraiz, J. Sheikh, Current perspectives, recent advancements, and efficiencies of various dye-containing wastewater treatment technologies, J. Water Process. Eng. 53 (2023) 103579.

[3] S. Benkhaya, S. M' rabet, A. El Harfi, A review on classifications, recent synthesis and applications of textile dyes, Inorg. Chem. Commun. 115 (2020) 107891.

[4] G.T. Şanlı, E. Demirhan, Preparation and characterization of chitosan/zeolite composites for Reactive Orange 122 dye removal from aqueous media: isotherm and kinetic studies, Biomass Convers, Biorefin, 2024.

[5] H. Aydin, Ç. Yerlikaya, Utilization of shells of hazelnut modified with Reactive Orange 122 as adsorbent for the removal of Cu(II), Desalin. Water Treat. 20 (2010) 123–132.

[6] M.M. El-Sheekh, A.R. El-Shanshoury, G.W. Abou-El-Souod, D.Y. Gharieb, S.M. El Shafay, Decolorization of dyestuffs by some species of green algae and cyanobacteria and its consortium, Int. J. Environ. Sci. Technol. 18 (2021) 3895–3906.

[7] M. Saeed, R. Nadeem, M. Yousaf, Removal of industrial pollutant (Reactive Orange 122 dye) using environment-friendly sorbent Trapa bispinosa's peel and fruit, Int. J. Environ. Sci. Technol. 12 (2015) 1223–1234.

[8] S. Ilhan, C.F. Iscen, N. Caner, I. Kiran, Biosorption potential of dried Penicillium restrictum for Reactive Orange 122: isotherm, kinetic and thermodynamic studies, J. Chem. Technol. Biotechnol. 83 (2008) 569–575.

[9] A. Siddique, I.A. Shaikh, A. Ali, S. Islam, A. Tariq, K. Ikram, Recycling of textile dyeing wash-off liquor using Fenton technology, Desalin. Water Treat. 212 (2021) 244–253.

[10] M.H.P. Santana, L.M. Da Silva, A.C. Freitas, J.F.C. Boodts, K.C. Fernandes, L.A. De Faria, Application of electrochemically generated ozone to the discoloration and degradation of solutions containing the dye Reactive Orange 122, J. Hazard. Mater. 164 (2009) 10–17.

[11] L.M.S. Colpini, G.G. Lenzi, M.B. Urio, D.M. Kochepka, H.J. Alves, Photodiscoloration of textile reactive dyes on Ni/TiO_2 prepared by the impregnation method: Effect of calcination temperature, J. Environ. Chem. Eng. 2 (2014) 2365–2371.

[12] S.A.D. Ferreira, J.F. Donadia, G.R. Gonçalves, A.L. Teixeira, M.B.J.G. Freitas, A.A. R. Fernandes, M.F.F. Lelis, Photocatalytic performance of granite waste in the decolorization and degradation of Reactive Orange 122, J. Environ. Chem. Eng. 7 (2019) 103144.

[13] L.M.S. Colpini, H.J. Alves, O.A.A.d. Santos, C.M.M. Costa, Discoloration and degradation of textile dye aqueous solutions with titanium oxide catalysts obtained by the sol–gel method, Dyes Pigm. 76 (2008) 525-529.

[14] K. Atrak, A. Ramazani, S. Taghavi Fardood, A novel sol–gel synthesis and characterization of $MgFe_2O_4$@γ–Al_2O_3 magnetic nanoparticles using tragacanth gel and its application as a magnetically separable photocatalyst for degradation of organic dyes under visible light, J. Mater. Sci.: Mater. Electron. 29 (2018) 6702–6710.

[15] M.I. Badawy, F.A. Mahmoud, A.A. Abdel-Khalek, T.A. Gad-Allah, A.A. Abdel Samad, Solar photocatalytic activity of sol–gel prepared Ag-doped ZnO thin films, Desalin. Water Treat. 52 (2014) 2601–2608.

[16] A.S. Ganie, S. Bano, N. Khan, S. Sultana, Z. Rehman, M.M. Rahman, S. Sabir, F. Coulon, M.Z. Khan, Nanoremediation technologies for sustainable remediation of contaminated environments: Recent advances and challenges, Chemosphere 275 (2021) 130065.

[17] A. Iqbal, A.S. Ahmed, N. Ahmad, A. Shafi, T. Ahamad, M.Z. Khan, S. Srivastava, Biogenic synthesis of CeO_2 nanoparticles and its potential application as an efficient photocatalyst for the degradation of toxic amido black dye, Environ. Nanotechnol. Monit. Manag. 16 (2021) 100505.

[18] C.V. Reddy, J. Shim, M. Cho, Synthesis, structural, optical and photocatalytic properties of CdS/ZnS core/shell nanoparticles, J. Phys. Chem. Solids 103 (2017) 209–217.

[19] S. Muzammal, A. Ahmad, M. Sheraz, J. Kim, S. Ali, M.B. Hanif, I. Hussain, S. Pandiaraj, A. Alodhayb, M.S. Javed, H.A.Z. Al-bonsrulah, M. Motola, Polymer-supported nanomaterials for photodegradation: Unraveling the methylene blue menace, Energy Conv. Manag.:x 22 (2024) 100547.

[20] A.S. Morshedy, E.M. El-Fawal, T. Zaki, A.A. El-Zahhar, M.M. Alghamdi, A.M.A. El Naggar, A review on heterogeneous photocatalytic materials: Mechanism, perspectives, and environmental and energy sustainability applications, Inorg. Chem. Commun. 163 (2024) 112307.

[21] X. Yang, D. Wang, Photocatalysis: From Fundamental Principles to Materials and Applications, ACS Appl. Energy Mater. 1 (2018) 6657–6693.

[22] A. Fatima, J. Akhtar, K.H. Thebo, M. Kazi, Enhanced Photocatalytic Degradation of Doxycycline over Titania under Visible Light, Arab. J. Sci, Eng, 2024.

[23] N. Turkten, B. Karatas, Y. Karatas, Z. Cinar, M. Bekbolet, A facile synthesis of bio-inspired hierarchical microstructure TiO_2: Characterization and photocatalytic activity, Environ. Prog. Sustain. Energy 42 (2023) e14054.

[24] S.S. Ghumro, B. Lal, T. Pirzada, M.A. Qazi, A. Ali, A.A. Altaf, K.H. Thebo, M. Kazi, Exploring the hetero-catalytic proficiencies of pristine and carbon-doped titania nanocatalysts in dye degradation and their synergetic profiles against bacteria, J. Mol. Struct. 1319 (2025) 139462.

[25] J.A. Buledi, A. Hyder, A. Ali, A.R. Solangi, A. Mallah, S. Amin, A.A. Memon, K. H. Thebo, M. Kazi, Strategic decolorization of rose bengal in an aqueous environment using a zinc oxide-loaded reduced graphene oxide photocatalyst, J. Phys. Chem. Solids 192 (2024) 112083.

[26] U. Khanum, M.K. Shabbir, Q.-u.-a. Shaikh, A. Ali, J. Akhtar, K.H. Thebo, J. Yangi, M. Kazi, Synthesis of graphene-based nanocomposites with superior doxycycline removal efficiency and antimicrobial studies, J. Photochem. Photobiol. A 456 (2024) 115865.

[27] M.K. Shabbir, J. Akhtar, K.H. Thebo, M. Kazi, Synthesis of highly efficient ternary phase graphene/Bi/SnO_2 photocatalyst for degradation of organic dye pollutants, Optik 304 (2024) 171734.

[28] A. Krishnan, A. Swarnalal, D. Das, M. Krishnan, V.S. Saji, S.M.A. Shibli, A review on transition metal oxides based photocatalysts for degradation of synthetic organic pollutants, J. Environ. Sci. 139 (2024) 389–417.

[29] S.C. Priya, S. Vijayalakshmi, S.G. Raghavendra, S. Yıldızhan, J. Ranjitha, A critical review on efficient photocatalytic degradation of organic compounds using copper-based nanoparticles, Materials Today: Proceedings 80 (2023) 3075-3081.

[30] M. Jeevarathinam, I.V. Asharani, Synthesis of CuO, ZnO nanoparticles, and CuO-ZnO nanocomposite for enhanced photocatalytic degradation of Rhodamine B: a comparative study, Sci. Rep. 14 (2024) 9718.

[31] A.K. Sibhatu, G.K. Weldegebrieal, S. Sagadevan, N.N. Tran, V. Hessel, Photocatalytic activity of CuO nanoparticles for organic and inorganic pollutants removal in wastewater remediation, Chemosphere 300 (2022) 134623.

[32] R. Djellabi, J. Ali, X. Zhao, A.N. Saber, B. Yang, CuO NPs incorporated into electron-rich TCTA@PVP photoactive polymer for the photocatalytic oxidation of dyes and bacteria inactivation, J. Water Process. Eng. 36 (2020) 101238.

[33] H. Aminzadeh, M. Shahabi Nejad, I. Mohammadzadeh, H. Sheibani, Assembly of CuO nanorods onto poly(glycidylmethacrylate)@polyaniline core–shell microspheres: Photocatalytic degradation of paracetamol, Appl. Organomet. Chem. n/a e6423.

[34] S. Iqbal, M. Javed, A. Bahadur, M.A. Qamar, M. Ahmad, M. Shoaib, M. Raheel, N. Ahmad, M.B. Akbar, H. Li, Controlled synthesis of Ag-doped CuO nanoparticles as a core with poly(acrylic acid) microgel shell for efficient removal of methylene blue under visible light, J. Mater. Sci.: Mater. Electron. 31 (2020) 8423–8435.

[35] A. Rani, M.K. Shabbir, A. Fatima, S. Ali, M. Alamzeb, A. Nadeem, J. Akhtar, A.M. Bejarani, K.H. Thebo, Visible Light-Triggered Catalytic Performance of Reduced Graphene Oxide Decorated With Copper Oxide Nanocomposite for Degradation of Rhodamine B Dye and Kinetics Studies, Microsc. Res. Tech. n/a.

[36] Z. Xiao, J. Xiao, Q. Sun, Y. Wang, L. Pan, C. Shi, X. Zhang, J.-J. Zou, Interface Engineering of Conjugated Polymer-Based Composites for Photocatalysis, Chemistry – A, European Journal 28 (2022) e202202593.

[37] C. Ergun, A Current Review on Conducting Polymer-Based Catalysts: Advanced Oxidation Processes for the Removal of Aquatic Pollutants, Water Air Soil Pollut. 234 (2023) 524.

[38] S. Raza, X. Li, F. Soyekwo, D. Liao, Y. Xiang, C. Liu, A comprehensive overview of common conducting polymer-based nanocomposites; Recent advances in design and applications, Eur. Polym. J. 160 (2021) 110773.

[39] N. Turkten, Y. Karatas, M. Bekbolet, Conducting Polymers and Photocatalysis: A Mini Review on Selected Conducting Polymers and Photocatalysts as TiO_2 and ZnO, Journal of Photocatalysis 2 (2021) 252–270.

[40] A. Kanwal, M. ur Rehman, R. Sattar, K.H. Thebo, M. Kazi, Highly efficient tin oxide and polyaniline-tin-oxide nanostructured materials for photocatalytic degradation of organic dyes, J. Mol. Struct. 1312 (2024) 138454.

[41] N. Ahmad, J. Anae, M.Z. Khan, S. Sabir, X.J. Yang, V.K. Thakur, P. Campo, F. Coulon, Visible light-conducting polymer nanocomposites as efficient photocatalysts for the treatment of organic pollutants in wastewater, J. Environ. Manage. 295 (2021) 113362.

[42] Z. Cui, R. Yuan, H. Chen, B. Zhou, B. Zhu, C. Zhang, Application of polyaniline-based photocatalyst in photocatalytic degradation of micropollutants in water: A review, J. Water Process. Eng. 59 (2024) 104900.

[43] A.L. Pang, A. Arsad, M.A. Ahmad Zaini, R. Garg, M. Saqlain Iqbal, U. Pal, M.A. S. Mohammad Haniff, A. Azlan Hamzah, S.-Y. Pung, M. Ahmadipour, A comprehensive review on photocatalytic removal of heavy metal ions by polyaniline-based nanocomposites, Chem. Eng. Commun. 211 (2024) 275–299.

[44] N.K. Jangid, S. Jadoun, A. Yadav, M. Srivastava, N. Kaur, Polyaniline-TiO_2-based photocatalysts for dyes degradation, Polym. Bull. 78 (2021) 4743–4777.

[45] J.A. Oyetade, R.L. Machunda, A. Hilonga, Photocatalytic degradation of azo dyes in textile wastewater by Polyaniline composite catalyst-a review, Sci. Afr. 17 (2022) e01305.

[46] N. Turkten, Y. Karatas, M. Bekbolet, Preparation of PANI Modified ZnO Composites via Different Methods: Structural, Morphological and Photocatalytic Properties, Water 13 (2021).

[47] N. Turkten, Y. Karatas, C.S. Uyguner-Demirel, M. Bekbolet, Preparation of PANI modified TiO_2 and characterization under pre- and post- photocatalytic conditions, Environ. Sci. Pollut. Res. 30 (2023) 111182–111207.

[48] C.S. Uyguner-Demirel, N. Turkten, Y. Karatas, M. Bekbolet, Photocatalytic performance of PANI modified TiO_2: Degradation of refractory organic matter, Environ. Sci. Pollut. Res. 30 (2023) 85626–85638.

[49] O. Koysuren, H.N. Koysuren, Application of CuO and its composite with polyaniline on the photocatalytic degradation of methylene blue and the Cr(VI) photoreduction under visible light, J. Sol-Gel Sci. Technol. 106 (2023) 131–148.

[50] H.N. Koysuren, O. Koysuren, Photocatalytic Activity of Boron Doped CuO and Its Composite with Polyaniline, Polym.-Plast. Technol. Mater. 62 (2023) 281–293.

[51] R. Nekooie, T. Shamspur, A. Mostafavi, Novel CuO/TiO_2/PANI nanocomposite: Preparation and photocatalytic investigation for chlorpyrifos degradation in water under visible light irradiation, J. Photochem. Photobiol. A 407 (2021) 113038.

[52] B.S. Rathore, N.P.S. Chauhan, M.K. Rawal, S.C. Ameta, R. Ameta, Chitosan–polyaniline–copper(II) oxide hybrid composite for the removal of methyl orange dye, Polym. Bull. 77 (2020) 4833–4850.

[53] T.B. Gelaw, B.K. Sarojini, A.K. Kodoth, Chitosan/Hydroxyethyl Cellulose Gel Immobilized Polyaniline/CuO/ZnO Adsorptive-Photocatalytic Hybrid Nanocomposite for Congo Red Removal, J. Polym. Environ. 30 (2022) 4086–4101.

[54] V.S. de Souza, H.O. da Frota, E.A. Sanches, Polyaniline-CuO hybrid nanocomposite with enhanced electrical conductivity, J. Mol. Struct. 1153 (2018) 20–27.

[55] A. Nafady, M.D. Albaqami, A.M. Alotaibi, CuO nanoparticles embedded in conductive PANI framework for periodic detection of alcohol from sweat, Colloid. Polym. Sci. 301 (2023) 517–526.

[56] P. Singh, S.K. Shukla, Structurally optimized cupric oxide/polyaniline nanocomposites for efficient humidity sensing, Surf. Interfaces 18 (2020) 100410.

[57] A.G.N. Sofiah, M. Samykano, S. Shahabuddin, K. Kadirgama, A.K. Pandey, A comparative experimental study on the physical behavior of mono and hybrid RBD palm olein based nanofluids using CuO nanoparticles and PANI nanofibers, Int. Commun. Heat Mass Transfer 120 (2021) 105006.

[58] S. Ammara, S. Noreen, S. Ali, S. Jamil, M.J. Bibi, S.R. Latif, Khan, CuO/PANI nanocomposite: an efficient catalyst for degradation and reduction of pollutants, Polym, Bull, 2024.

[59] B. Zhang, F. Shang, X. Shi, R. Yao, F. Wei, X. Hou, W. Li, J. Zhang, Polyaniline/CuO Nanoparticle Composites for Use in Selective H_2S Sensors, ACS Appl. Nano Mater. 6 (2023) 18413–18425.

[60] M. Rahim, A.-U.-H.-A. Shah, S. Bilal, I. Rahim, R. Ullah, Highly Efficient Humidity Sensor Based on Sulfuric Acid Doped Polyaniline-Copper Oxide Composites, Iran. J. Sci. Technol. Trans. A: Sci. 45 (2021) 1981–1991.

[61] M.O. Ansari, M. Oves, N. Salah, M. Asad, R. Kumar, P.M.Z. Hasan, A. Alshahrie, R. Darwesh, DC electrical conductivity retention and antibacterial aspects of microwave-assisted ultrathin CuO@polyaniline composite, Chem. Pap. 74 (2020) 3887–3898.

[62] M.B. Gholivand, H. Heydari, A. Abdolmaleki, H. Hosseini, Nanostructured CuO/PANI composite as supercapacitor electrode material, Mater. Sci. Semicond. Process. 30 (2015) 157–161.

[63] C. L, P. S, CuO-PANI nanostructure with tunable spectral selectivity for solar selective coating application, Appl. Surf. Sci. 378 (2016) 245-252.

[64] N. Kumar, N.C. Joshi, Adsorption applications of synthetically prepared PANI-CuO based nanocomposite material, J. Indian Chem. Soc. 99 (2022) 100551.

[65] N. Maruthi, M. Faisal, N. Raghavendra, B.P. Prasanna, S.R. Manohara, M. Revanasiddappa, Anticorrosive polyaniline-coated copper oxide (PANI/CuO) nanocomposites with tunable electrical properties for broadband electromagnetic interference shielding, Colloids Surf A Physicochem Eng Asp 621 (2021) 126611.

[66] M. Nagaraja, S. Prashanth, J. Pattar, H.M. Mahesh, K. Rajanna, Polyaniline-CuO nanocomposite: Electrical, structural and sensor properties, Materials Today: Proceedings 49 (2022) 1989-1992.

[67] Y.Y. Gurkan, N. Turkten, A. Hatipoglu, Z. Cinar, Photocatalytic degradation of cefazolin over N-doped TiO_2 under UV and sunlight irradiation: Prediction of the reaction paths via conceptual DFT, Chem. Eng. J. 184 (2012) 113–124.

[68] N. Turkten, Z. Cinar, Photocatalytic decolorization of azo dyes on TiO_2: Prediction of mechanism via conceptual DFT, Catal. Today 287 (2017) 169–175.

[69] P. Scherrer, Estimation of the size and internal structure of colloidal particles by means of röntgen, Nachr. Ges. Wiss. Gottingen 2 (1918) 96–100.

[70] M. J. Frisch, G. W. Trucks, H. B. Schlegel, G. E. Scuseria, M. A. Robb, J. R. Cheeseman, G. Scalmani, V. Barone, G. A. Petersson, H. Nakatsuji, X. Li, A.M. M. Caricato, B.G.J. J. Bloino, R. Gomperts, B. Mennucci, H. P. Hratchian, J. V. Ortiz, A. F. Izmaylov, J. L. Sonnenberg, D. Williams-Young, F. Ding, F. Lipparini, F. Egidi, J. Goings, B. Peng, T.H. A. Petrone, D. Ranasinghe, V. G. Zakrzewski, J. Gao, N. Rega, G. Zheng, W. Liang, M. Hada, M. Ehara, K. Toyota, R. Fukuda, J. Hasegawa, M. Ishida, T. Nakajima, Y. Honda, O. Kitao, H. Nakai, K.T. T. Vreven, J. A. Montgomery, J.E.P. Jr., F. Ogliaro, M. Bearpark, E.B. J. J. Heyd, K. N. Kudin, V. N. Staroverov, R.K. T. Keith, K.R. J. Normand, A. Rendell, J. C. Burant, S. S. Iyengar, J. Tomasi, M. Cossi, J. M. Millam, M. Klene, C. Adamo, R. Cammi, J. W. Ochterski, R. L. Martin, K. Morokuma, O. Farkas, J. B. Foresman, a.D.J. Fox, Gaussian 09, Revision A.02, Gaussian, Inc., Wallingford CT, 2016.

[71] A.D. Becke, Density-functional thermochemistry. III. The role of exact exchange, J. Chem. Phys. 98 (1993) 5648–5652.

[72] M.J. Frisch, J.A. Pople, J.S. Binkley, Self-consistent molecular orbital methods 25, Supplementary Functions for Gaussian Basis Sets, the Journal of Chemical Physics 80 (1984) 3265–3269.

[73] P. Geerlings, F. De Proft, W. Langenaeker, Conceptual Density Functional Theory, Chem. Rev. 103 (2003) 1793–1874.

[74] Y. Deng, L. Tang, G. Zeng, H. Dong, M. Yan, J. Wang, W. Hu, J. Wang, Y. Zhou, J. Tang, Enhanced visible light photocatalytic performance of polyaniline modified mesoporous single crystal TiO_2 microsphere, Appl. Surf. Sci. 387 (2016) 882–893.

[75] M. Trchová, J. Stejskal, Polyaniline: The infrared spectroscopy of conducting polymer nanotubes (IUPAC Technical Report), Pure Appl. Chem. 83 (2011) 1803–1817.

[76] Z. Ping, In situ FTIR–attenuated total reflection spectroscopic investigations on the base–acid transitions of polyaniline. Base–acid transition in the emeraldine form of polyaniline, J. Chem. Soc., Faraday Trans. 92 (1996) 3063–3067.

[77] J. Stejskal, I. Sapurina, Polyaniline — A Conducting Polymer, in: U. Schubert, N. Hüsing, R.M. Laine (Eds.), Materials Syntheses: A Practical Guide, Springer Vienna, Vienna, 2008, pp. 199–207.

[78] K. Borgohain, J.B. Singh, M.V. Rama Rao, T. Shripathi, S. Mahamuni, Quantum size effects in CuO nanoparticles, Phys. Rev. B 61 (2000) 11093–11096.

[79] H. Fu, S. Shewfelt, L.D. Sylvan, J.-F. Gaillard, K.A. Gray, Polyaniline-metal oxide coatings for biocidal applications: Mechanisms of activation and deactivation, Chemosphere 346 (2024) 140543.

[80] S. Tao, B. Hong, Z. Kerong, An infrared and Raman spectroscopic study of polyanilines co-doped with metal ions and H^+, Spectrochim Acta A Mol Biomol Spectrosc 66 (2007) 1364–1368.

[81] A.A. Nekrasov, O.L. Gribkova, O.D. Iakobson, I.N. Ardabievskii, V.F. Ivanov, A. V. Vannikov, Raman spectroelectrochemical study of electrodeposited polyaniline doped with polymeric sulfonic acids of different structures, Chem. Pap. 71 (2017) 449–458.
[82] M.S. Sengar, S. Saxena, S.P. Satsangee, R. Jain, CuO decorated polyaniline nanocomposite-based sensor for the electrochemical determination of an opioid analgesic, Ionics 28 (2022) 903–918.
[83] I. Šeděnková, M. Trchová, J. Stejskal, Thermal degradation of polyaniline films prepared in solutions of strong and weak acids and in water – FTIR and Raman spectroscopic studies, Polym. Degrad. Stab. 93 (2008) 2147–2157.
[84] S. Zhu, M. Wu, M.-H. Ge, H. Zhang, S.-K. Li, C.-H. Li, Design and construction of three-dimensional CuO/polyaniline/rGO ternary hierarchical architectures for high performance supercapacitors, J. Power Sources 306 (2016) 593–601.
[85] J. Stejskal, A. Riede, D. Hlavatá, J. Prokeš, M. Helmstedt, P. Holler, The effect of polymerization temperature on molecular weight, crystallinity, and electrical conductivity of polyaniline, Synth. Met. 96 (1998) 55–61.
[86] L.V. Devi, T. Selvalakshmi, S. Sellaiyan, A. Uedono, K. Sivaji, S. Sankar, Effect of La doping on the lattice defects and photoluminescence properties of CuO, J. Alloys Compd. 709 (2017) 496–504.
[87] M. Radoičić, Z. Šaponjić, I.A. Janković, G. Ćirić-Marjanović, S.P. Ahrenkiel, M. I. Čomor, Improvements to the photocatalytic efficiency of polyaniline modified TiO_2 nanoparticles, Appl. Catal. B 136–137 (2013) 133–139.
[88] A. Verma, T. Kumar, Gas sensing properties of a Cu-doped PANI nanocomposite towards ammonia, Mater. Adv. 5 (2024) 7387–7400.
[89] S. Paneru, D. Kumar, A Novel Electrochemical Biosensor Based on Polyaniline-Embedded Copper Oxide Nanoparticles for High-Sensitive Paraoxon-Ethyl (PE) Detection, Appl. Biochem. Biotechnol. 195 (2023) 4485–4502.
[90] R. Ullah, S. Bilal, K. Ali, A.-u.-H.A. Shah, Synthesis and characterization of polyaniline doped with Cu II chloride by inverse emulsion polymerization, Synth. Met. 198 (2014) 113-117.
[91] K. Pandey, P. Yadav, I. Mukhopadhyay, Elucidating the effect of copper as a redox additive and dopant on the performance of a PANI based supercapacitor, PCCP 17 (2015) 878–887.
[92] K.S.W. Sing, Reporting physisorption data for gas/solid systems with special reference to the determination of surface area and porosity (Recommendations 1984), Pure Appl. Chem. (1985) 603.
[93] A. Ramadan, M. Anas, S. Ebrahim, M. Soliman, A.I. Abou-Aly, Polyaniline/fullerene derivative nanocomposite for highly efficient supercapacitor electrode, Int. J. Hydrogen Energy 45 (2020) 16254–16265.
[94] A. Moyseowicz, G. Gryglewicz, Hydrothermal-assisted synthesis of a porous polyaniline/reduced graphene oxide composite as a high-performance electrode material for supercapacitors, Compos. B Eng. 159 (2019) 4–12.
[95] Y. Xu, B. Liu, C. Dong, H. Feng, Y. Wei, X. Zhang, High-performance Flexible Symmetric Supercapacitor Based on Heterostructured PANI@MoS_2 Nanocomposite Electrode, Eur. J. Inorg. Chem. 26 (2023) e202200569.
[96] S. Yurdakal, C. Garlisi, L. Özcan, M. Bellardita, G. Palmisano, Chapter 4 - (Photo) catalyst Characterization Techniques: Adsorption Isotherms and BET, SEM, FTIR, UV–Vis, Photoluminescence, and Electrochemical Characterizations, in: G. Marcì, L. Palmisano (Eds.) Heterogeneous Photocatalysis, Elsevier 2019, pp. 87-152.
[97] E.C. Gomes, M.A.S. Oliveira, Chemical Polymerization of Aniline in Hydrochloric Acid (HCl) and Formic Acid (HCOOH) Media. Differences Between the Two Synthesized Polyanilines, J. Appl. Polym. Sci. 2 (2012) 5–13.
[98] S.K. Singh, R.K. Shukla, R. Kumar, U.K. Tripathi, S.K. Mishra, Investigation on PANI/CuO nanocomposites for ammonia gas sensing applications, Mater. Lett. 309 (2022) 131325.
[99] G.E. do Nascimento, D.C. Napoleão, P.K. de Aguiar Silva, R.M. da Rocha Santana, A.M.R. Bastos, L.E.M.C. Zaidan, M.C. de Moura, L.C.B.B. Coelho, M.M.M.B. Duarte, Photo-Assisted Degradation, Toxicological Assessment, and Modeling Using Artificial Neural Networks of Reactive Gray BF-2R Dye, Water Air Soil Poll. 229 (2018) 379.
[100] R. Khan, M.A. Inam, D.R. Park, S. Khan, M. Akram, I.T. Yeom, The Removal of CuO Nanoparticles from Water by Conventional Treatment C/F/S: The Effect of pH and Natural Organic Matter, Molecules 24 (2019) 914.
[101] H. Li, W. Huang, B. Qiu, H.K. Thabet, D. Alhashmialameer, M. Huang, Z. Guo, Effective removal of proteins and polysaccharides from biotreated wastewater by polyaniline composites, Adv. Compos. Hybrid Mater. 5 (2022) 1888–1898.
[102] S. Safa, R. Azimirad, S. Safalou Moghaddam, M. Rabbani, Investigating on photocatalytic performance of CuO micro and nanostructures prepared by different precursors, Desalin. Water Treat. 57 (2016) 6723–6731.
[103] R. Riaz, I. Bibi, F. Majid, S. Kamal, M.A. Huwayz, K. Jilani, A. Ghafoor, Q. Raza, N. Alwadai, M. Iqbal, $NiFe_2O_4$/CuO heterostructures optical, magnetic and photocatalytic properties: Methylene blue dye degradation under solar light irradiation, J. Mol. Struct. 1309 (2024) 138174.
[104] M. Stylidi, D.I. Kondarides, X.E. Verykios, Visible light-induced photocatalytic degradation of Acid Orange 7 in aqueous TiO_2 suspensions, Appl. Catal. B 47 (2004) 189–201.
[105] I. Toumi, H. Djelad, F. Chouli, A. Benyoucef, Synthesis of PANI@ZnO Hybrid Material and Evaluations in Adsorption of Congo Red and Methylene Blue Dyes: Structural Characterization and Adsorption Performance, JJ. Inorg. Organomet. Polym. Mater. 32 (2022) 112–121.
[106] A.S. Özen, V. Aviyente, R.A. Klein, Modeling the Oxidative Degradation of Azo Dyes: A Density Functional Theory Study, J. Phys. Chem. A 107 (2003) 4898–4907.
[107] A.M. Elhorri, K.D. Belaid, M. Zouaoui-Rabah, R. Chadli, Theoretical study of the azo dyes dissociation by advanced oxidation using Fukui indices. DFT calculations, Comput, Theor. Chem. 1130 (2018) 98–106.
[108] N. Kaur, S. Kaur, V. Singh, Preparation, characterization and photocatalytic degradation kinetics of Reactive Red dye 198 using N, Fe codoped TiO_2 nanoparticles under visible light, Desalin. Water Treat. 57 (2016) 9237–9246.

Yunus Karatas is currently a researcher at Kirsehir Ahi Evran University. He received his PhD degree in Chemistry from the Westfaelische Wilhelms-Universitaet Münster, Germany in 2006. His main research interests include lithium-ion batteries, polymer electrolytes, synthesis of polyposphazene and polysiloxane, conducting polymers, polymer composites and photocatalysis.